Nonlinear Networks for Arbitrary Optical Synthesis

Jennifer A. Black,[1,*] Zachary L. Newman,[1,2] Su-Peng Yu,[1,3] David R. Carlson,[1,2] and Scott B. Papp[1,3]

[1]*Time and Frequency Division, National Institute of Standards and Technology, Boulder, Colorado 80305, USA*

[2]*Octave Photonics, Louisville, Colorado 80027, USA*

[3]*Department of Physics, University of Colorado, Boulder, Colorado 80302, USA*

(Received 30 August 2022; revised 8 March 2023; accepted 27 April 2023; published 19 May 2023)

Nonlinear wavelength conversion is a powerful control of light, especially when implemented at the nanoscale with integrated photonics. However, strict energy conservation and phase-matching requirements constrain the converted output. To overcome these constraints and enable novel functionalities, we introduce nonlinear networks—systems of nonlinear photonic elements that observe a programmable set of conservation rules. We highlight the diverse capabilities of nonlinear networks by demonstrating an optical-frequency synthesizer, which operates at nearly arbitrary output frequency exceeding the state of the art in synthesized conversion bandwidth. Using a codesigned microresonator network, our synthesizer is based on four-wave mixing (FWM) spectral translation of a tunable laser and a frequency comb. Energy conservation in FWM provides deterministic synthesis, and it allows a nearly arbitrary frequency tuning range by the dependence of resonant FWM on group-velocity dispersion, temperature, and input laser frequency. Moreover, we take advantage of efficient parametric amplification intrinsic to nonlinear networks. We operate spectral translation across output ranges up to 200 THz, and we characterize the synthesizer through precise metrology, demonstrating < 0.1 Hz absolute accuracy. Our experiments introduce nonlinear networks that perform complex functionalities, including optical synthesis with nearly limitless bandwidth.

DOI: 10.1103/PhysRevX.13.021027 Subject Areas: Photonics

I. INTRODUCTION

Nonlinear optics is a field of ubiquitous matured technologies, such as frequency doubling, yet it still offers space for novel experiments and innovation toward realizing the technologies of tomorrow. With nonlinear optics, there exist several modes of interaction between light and material, yielding vastly different scenarios for frequency conversion. For example, second-harmonic, high-harmonic, and sum- and difference-frequency generation involve input photons that are destroyed in adding up to a new, higher energy photon. Another mode is optical-parametric oscillation (OPO) in which input light is shifted to outputs at fundamentally new frequencies. Yet another mode is four-wave mixing (FWM) in which two inputs multiply cascade into pairs of outputs with precisely balanced energy. All these distinct nonlinear modes require both energy and momentum conservation, which we denote as phase matching of the input and output light. The stringent constraint of phase matching alongside the inherent weakness of nonlinearity perfectly maintain coherence in nonlinear conversion, but they severely restrict the choice of input and output frequency. As an example, generating a variable output frequency could be accomplished by concatenating the frequency shift possible with OPO and the deterministic frequency cascade of FWM.

Traditional nonlinear optics is now a robust tool to create colors of light for research well beyond the optical sciences, extending to laser measurements in biology [1], gravitational-wave detection [2], geodesy [3], analysis of chemical reactions [4], and clocks and standards research [5]. In particular, laser-frequency stabilization and synthesis relies on nonlinear optics for supercontinuum generation, self-referencing, and laser conversion with harmonic and difference generation [6,7]. Nonlinear networks, with an expanded palette of operations that come from combining phase matching in discrete elements, can not only enhance possibilities with frequency conversion but also open arbitrary paths for amplitude, phase, and frequency processing of light inputs. Hence, nonlinear networks could expand existing uses of nonlinear optics, and they expand the design space of nonlinear phase matching to explore

*Corresponding author.
jennifer.black@nist.gov

new interactions and develop new applications. Integrated photonics, which enables complex and powerful circuits of light, is an ideal setting to explore nonlinear networks due to high material Kerr or quadratic nonlinearity and strong confinement, robust controls of phase matching through geometry [8] and nanoscale patterns [9], and the continuing push to include integrated photonics in semiconductor foundries promises scalable access. Nonlinear networks will not only explore interesting new regimes of nonlinear dynamics and complex systems, but will also address future technologies in generating and processing useful signals with light.

Frequency synthesis is the generation of oscillatory signals with precisely calibrated frequency and phase, derived by an input reference clock, whose fractional-frequency stability is maintained. It is essential in modern electronics, such as for digital computing, cell phone networks, and positioning and navigation with the Global Positioning System. Frequency synthesizers in the electronic domain are robust, widely available, and operate seamlessly across the entire radio frequency to millimeter-wave range. Use of the optical domain promises fundamental performance enhancement over electronics, including enhanced bandwidth capacity, quantum-limited measurements, and energy efficiency. Moreover, synthesized optical frequencies can function as rulers, referenced directly to International System of Units (SI) standards, for the most precise measurements possible, including for optical clocks [10], transfer and sensing of timing signals [11], and detection of chemical and biological substances in the gas, liquid, and solid phase [12]. However, more than one technological leap will be required before optical synthesis reaches the level of nonexpert use that defines electronics. In parallel to the electronic case, an optical-frequency synthesizer [13] is a laser with its frequency calibrated by an optical-frequency comb, which is itself an array of lasers with precise frequency spacing [14]. To implement the optical synthesizer, one photodetects a heterodyne beat note between the tunable laser and the optical-frequency comb and uses it to program the synthesizer output via a phase-lock loop. Even though the optical domain provides enormous bandwidth, it is not currently possible for any tunable laser or frequency comb to reach even a fraction of the available bandwidth. Therefore, the output of an optical synthesizer is constrained by the extensible range of the tunable laser and optical-frequency comb, where most often the tunable laser-frequency range is the limiting factor.

Integrated photonics are an ideal setting to explore nonlinear optics. This is because integrated photonic elements such as lasers, amplifiers, waveguides, resonators, and metasurfaces operate with low loss across huge bandwidths and enable unparalleled nonlinearity and flexible phase matching for reconfigurable nonlinear processes. More specifically, waveguide-based microresonators provide resonant field enhancement with high quality factor, small mode volume, and group-velocity-dispersion (GVD) engineering for user-defined, resonant phase matching. Indeed, highly efficient FWM in microresonators provides a proven mechanism to generate soliton frequency combs, or simply microcombs [15], from a single continuous-wave (cw) input laser. Octave-spanning microcombs [16–18] based on precise GVD engineering in waveguides have been developed, and they have enabled microcomb optical synthesis [19,20] and clock [21,22] demonstrations. Besides microcomb generation that involves many resonator modes, optical-parametric oscillation and FWM, which involve only three cavity modes, are useful for spectral translation of a laser from one frequency to another [23–27]. With advancing GVD engineering techniques, the span of FWM spectral translation can exceed one octave to cover at least the near infrared, and the fundamental conversion efficiency reaches $> 10\%$, consistent with OPO in microresonators [28–34]. The frequencies of a microcomb are $\nu_\mu = \nu_0 + \mu f_{\text{rep}}$, where ν_0 is the pump frequency, μ is the mode order relative to $\mu = 0$, the pump mode, and f_{rep} is the repetition frequency, a microwave frequency determined by the microresonator size. The spectrum of an OPO consists of pump, signal, and idler frequencies, according to $2\nu_p = \nu_s + \nu_i$, and we represent spectral translation via FWM by $\nu_s = 2\nu_p - \nu_i$ in which independent lasers provide the pump and idler where the idler can be either higher or lower frequency than the pump. By leveraging the above capabilities of microresonators in nonlinear networks, we can overcome the constraints of single nonlinear elements to create novel chip-scale devices for generating high-precision, user-defined coherent outputs with unparalleled wavelength access. Moreover, existing foundry level technological ecosystems provide a path toward seamless integration of nonlinear networks on a single chip.

Here, we implement a nonlinear network for the purpose of arbitrary optical-frequency synthesis. By leveraging the nonlinear network, we overcome limitations of existing optical synthesizers to enable state-of-the-art output frequency range on a chip-scale platform. Our synthesizer uses one microresonator to generate a microcomb and a separate microresonator to implement spectral translation, involving the microcomb mode μ_T with frequency ν_{μ_T} and a pump laser of frequency ν_p. We test the attributes of our synthesizer architecture, especially through connections in the microresonator nonlinear network that fundamentally enable a much wider output frequency range than could be contemplated with previously described combs and tunable lasers. We explore the synthesizer's capability for broadband and user-defined tuning, especially the frequency step size that we vary over an extraordinary range from 0.1 Hz to 200 THz to cover vastly different frequency bands.

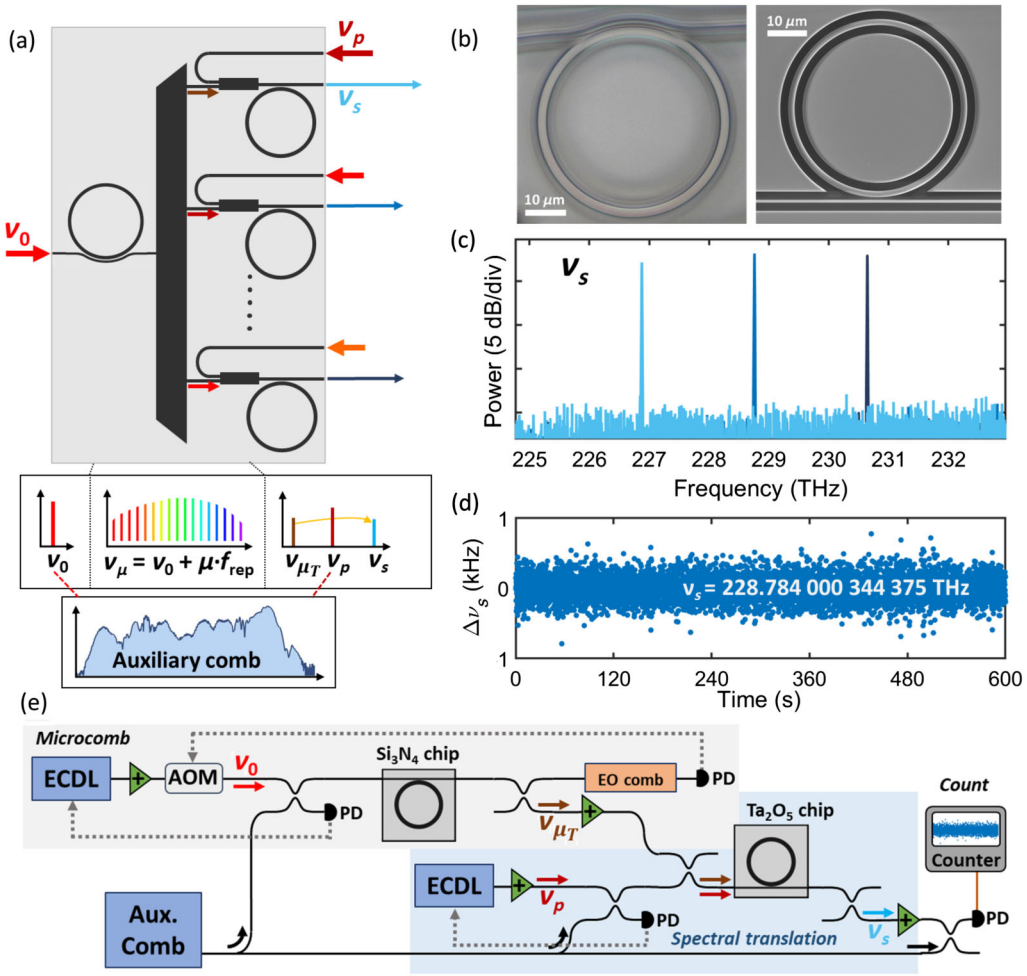

FIG. 1. Accurate and precise optical-frequency synthesizer by spectral translation. (a) Concept of a single-chip network that implements optical synthesis. A cw pump laser ν_0 generates a microcomb; modes are demultiplexed and spectrally translated in a second microresonator using a cw pump laser with frequency ν_p. (b) Image (left) and electron microscope image (right) of the SiN and tantala microresonators. (c) Optical-frequency-synthesizer output with tuning of 4 THz (22 nm). (d) Measured synthesis error $\Delta\nu_s$ (gate time 100 ms). (e) Schematic of the experimental setup. Two external-cavity diode lasers (ECDL) pump the microcomb (ν_0) and spectral-translation (ν_p) chips. Photodiodes (PD) measure various optical heterodyne beat note signals for relevant feedback phase locks (dashed gray lines) and for optical counting. Amplifiers (+) are used to overcome losses in the system and the auxiliary comb (Aux. Comb) is used for locking and counting. We control the microcomb f_{rep} by feedback to the optical pump power with an acousto-optic modulator (AOM), and we measure it by use of an electro-optic comb (EO comb) to create a photdetectable signal.

Incorporating additional nonlinear photonic elements to our synthesizer architecture would enable, for example, multiplexed operation, providing multiple deterministic output optical frequencies from a single chip.

II. CONCEPT

We implement the optical synthesizer according to the nonlinear microresonator network schematic in Fig. 1(a), which highlights microcomb wavelength multiplexing to seed different spectral-translation microresonators. Perfect phase matching for spectral translation requires $\Delta\beta = 2\beta_p - \beta_i - \beta_s = 0$ for the wave vectors of the pump β_p, the idler β_i, closely linked to the microcomb mode μ_T that is involved with spectral translation, and the mode associated with the synthesized laser β_s. We derive $\nu_s = \nu_0 + 2(\mu_p f_{\mathrm{rep}} + \delta) - \mu_T f_{\mathrm{rep}}$ for the synthesized output frequency, where the middle term in parentheses represents the spectral translation pump-laser frequency ν_p that is offset locked at a frequency δ from the microcomb mode μ_p. By stabilizing ν_0, f_{rep}, and δ with respect to a microwave reference clock, the stability of the clock is phase-coherently transferred to ν_s (see Appendix D). Operationally, we design for a choice of ν_s by adjusting the mode numbers μ_p and μ_T, and the GVD of the spectral translation microresonator. Moreover, the microcomb f_{rep} is a critical choice; we utilize a 1.002 THz microcomb architecture proven for self-referencing and optical-frequency metrology [18,19]. In any mode of operation,

the possibility to subdivide a large microcomb f_{rep} like 1 THz [19,21] or the use of ultrahigh speed photodetectors and electronics is an important system-design trade-off. Indeed, in our experiments we electro-optically modulate a portion of the microcomb spectrum in the 1550 nm band for phase stabilization of f_{rep} by feedback to the microcomb pump power (see Appendix B). Since FWM conserves energy and hence the phase coherence of the microcomb with respect to the reference clock, we anticipate zero error in the synthesized frequency. However, this is a feature of utmost importance and previously unexplored. Therefore, we characterize the output of our spectral translation optical-frequency synthesizer in detail by using an auxiliary erbium-fiber frequency comb (see Appendix B) for unambiguous verification of the synthesized laser output at ν_s. Our spectral-translation synthesizer [Fig. 1(a)] nonlinear network can be realized in various microresonator configurations, including with a single chip because microcomb generation and spectral translation are optimized with essentially the same device-layer thickness. We implement the microcomb with the silicon nitride (Si_3N_4, hereafter SiN) and spectral translation with the tantalum pentoxide platform [8,35,36] (Ta_2O_5, hereafter tantala) as shown in Fig. 1(b) (see Appendix A). The use of two materials demonstrates that nonlinear networks can be implemented with various integrated photonic platforms. Moreover, the same tantala thickness we use for spectral translation can support microcomb generation [35], yielding a path toward a single fully integrated nonlinear network.

We demonstrate and characterize our spectral-translation synthesizer primarily by its operation of generating a coherent laser output while supporting an exceptionally wide frequency tuning range. Figure 1(c) demonstrates the optical spectrum of the synthesizer as we step the output laser frequency ν_s in 2 THz increments through the 1300 nm band. In this experiment, we utilize the same microcomb mode with $\nu_{\mu_T} = 153.868\,324\,346\,250$ THz, yet we create widely separated outputs by varying the ring waveguide width of the spectral translation device to change FWM phase matching. Here, the output power of the synthesizer is optimized by minimization of system losses between the chips and thermal tuning of the spectral-translation microresonator, and we generate a sufficient output power for ultraprecise optical-frequency metrology. Naturally, the precision we obtain with ν_s depends exclusively on phase stabilization of the microcomb and ν_p, but conversion efficiency depends on design and fabrication tolerance of the microresonators, which we estimate corresponds to a 10 GHz precision in ν_s. Furthermore, we characterize the absolute optical-frequency-synthesis accuracy by measuring ν_s with the auxiliary frequency comb (see Appendix D). We form an optical heterodyne beat note with the synthesizer output and the auxiliary comb and record this frequency with a zero-dead-time frequency counter at 0.1 s gate. Figure 1(d) presents the absolute synthesizer frequency error $\Delta\nu_s = \nu_b - \nu_s$, where ν_b is the synthesized optical frequency that we measure with the auxiliary comb. In particular, $\nu_b = f_{\mathrm{CEO}} + n_b f_{\mathrm{rep,aux}} + \zeta$, where f_{CEO} and $f_{\mathrm{rep,aux}}$ are the auxiliary comb carrier-envelope offset frequency and repetition frequency of 30 and 250 MHz, respectively, n_b is an integer, and ζ is a microwave frequency measured by optical heterodyne of the synthesizer output with the auxiliary comb. Our measurements demonstrate $\Delta\nu_s = +0.035$ Hz in 10 min of continuous measurement consistent with zero synthesis error. These results verify subhertz accuracy of FWM, phase stabilization of the pump lasers and microcomb, and contributions from the auxiliary comb measurement system. Figure 1(e) presents a schematic of the experimental setup we use to demonstrate the nonlinear network for broadband optical-frequency synthesis, including microcomb generation, spectral translation, and ν_s counting with the auxiliary comb; see Appendix D for more details.

III. WAVELENGTH ACCESS THROUGH GVD ENGINEERING

Frequency agility, especially by reliable design of FWM and OPO in nonlinear networks, is the key advantage of our synthesizer. Figure 2 explores spectral translation over an optical bandwidth of ≈200 THz and ultraprecise frequency synthesis across the 1300 nm band. Both the microcomb and spectral-translation microresonators operate in the anomalous GVD regime in the frequency range of ν_0 and ν_p, and we design primarily the third- and fourth-order GVD contributions through adjusting the radius (R) and waveguide width (RW) of our resonators; see Fig. 2(a) (see Appendix C). In brief, we design the GVD of the microcomb to have zero-crossing wavelengths to generate dispersive waves [37] with one located at ν_{μ_T}, and we design the GVD of the spectral-translation device for energy and momentum conservation at ν_{μ_T} and ν_s with pump frequency ν_p. The integrated GVD describes deviations of a microresonator's free-spectral range $D_1/2\pi$ at ν_p with mode order $\mu = 0$ [15],

$$\begin{aligned} D_{\mathrm{int}} &= \omega - (\omega_0 + D_1\mu) \\ &= \frac{D_2\mu^2}{2!} + \frac{D_3\mu^3}{3!} + \frac{D_4\mu^4}{4!} + \cdots. \end{aligned} \tag{1}$$

We estimate the dispersive-wave wavelengths by solving the quadratic equation $D_{\mathrm{int}}(\mu_{\mathrm{DW}}) = 0$ [see Eq. (1)], yielding $\mu_{\mathrm{DW}} = -(2D_3)/D_4 \pm \sqrt{[(2D_3)/D_4]^2 - [(12D_2)/D_4]}$. Similarly, energy and momentum conservation enable efficient spectral translation, requiring $D_{\mathrm{int}}(\mu_{\mathrm{ST}}) = -D_{\mathrm{int}}(-\mu_{\mathrm{ST}})$ that results in the relationship $\mu_{\mathrm{ST}} = \sqrt{(-12D_2)/D_4}$. Comparing these estimates to results from our experiments is quite instructive as to the frequency determinism of our synthesizer architecture: specifically, the dispersive-wave

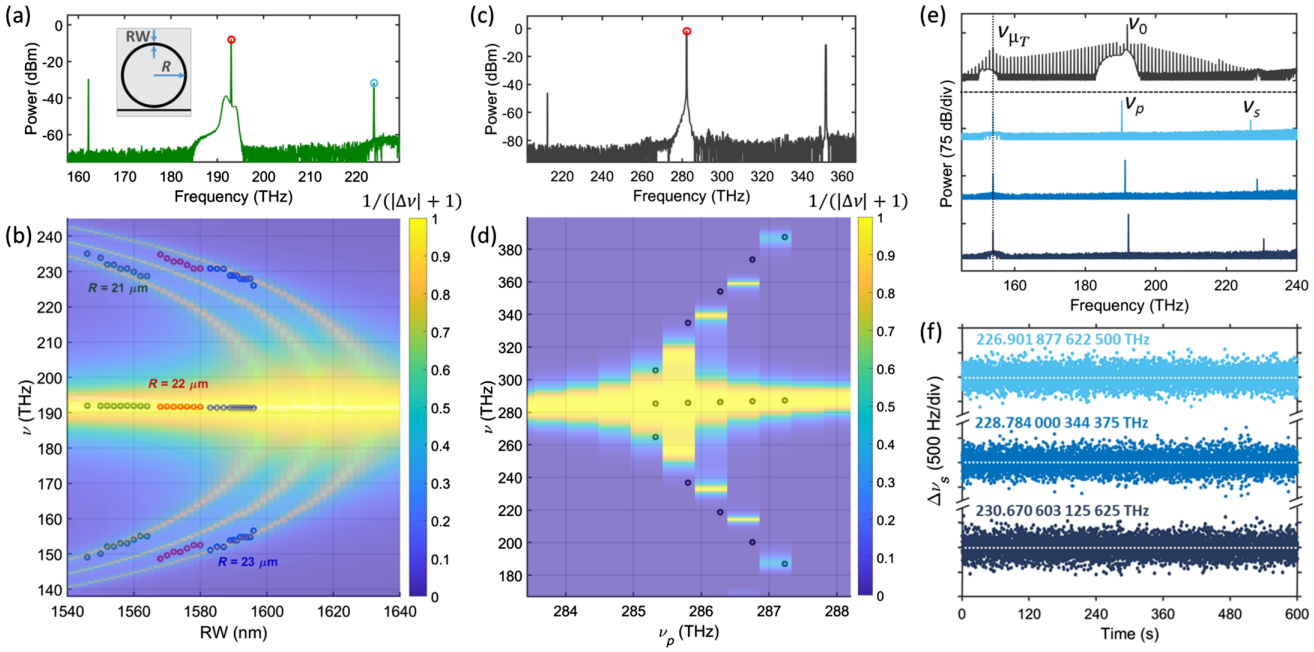

FIG. 2. GVD engineering of spectral translation for broadband optical synthesis. (a) Optical spectrum demonstrating efficient spectral translation from 223.7 to 162.1 THz in a device with $R = 21$ μm and RW $= 1.55$ μm. Red and blue circles denote the input frequencies. Inset schematic shows the lithographically tunable geometric parameters R and RW. (b) Green, red, and blue circles denote experimental $\nu_{(s,p,i)}$ for $R = 21$, 22, and 23 μm as a function of RW. Heat maps denote $1/(|\Delta\nu| + 1)$. (c) Optical spectrum demonstrating OPO in a device with $R = 45$ μm and RW $= 1.195$ μm. The red circle denotes the input frequency. (d) Experimental $\nu_{(s,p,i)}$ for $R = 45$ μm and RW $= 1.17$ μm as a function of ν_p. (e) Stacked optical spectra of the microcomb and the spectral translation of a single comb tooth (ν_{μ_T}) to three different frequencies (ν_s) by varying RW. (f) Measured $\Delta\nu_s$ (gate time 100 ms) of the synthesizer outputs.

and spectral-translation modes $\mu_{\mathrm{DW}} = -38$ and $\mu_{\mathrm{ST}} = 40$ are in reasonable agreement with microresonator parameter tolerances for $\nu_0 = 192$ THz and $\nu_p = 191$ THz; see Appendix A.

Figures 2(a) and 2(b) present spectral-translation characterization with a tunable, 1300 nm probe laser and the ν_p laser in the 1550 nm wavelength range (see Appendix B). Figure 2(a) shows a typical spectral-translation spectrum, and Fig. 2(b) is a heat map that indicates $1/(|\Delta\nu| + 1)$, where $\Delta\nu = 2\nu_p - \nu_s - \nu_p$, which we calculate at perfectly phase-matched modes in the resonator ($\Delta\beta = 0$). Therefore, $\Delta\nu = 0$ denotes theoretically perfect FWM frequency and phase matching in the resonator, necessary for optimizing parametric gain. To generate an output at any wavelength within our target ≈1270–1330 nm band with a microresonator on a fixed device-layer thickness, we primarily vary RW and use R for fine-tuning. In Fig. 2(b), the overlay data explore the difference-frequency dependence of ν_s and ν_i at peak parametric gain, determined by measured optimal four-wave mixing conversion efficiency, as a function of RW with a constant ν_p, and we demonstrate the sensitivity of GVD engineering to R; see Appendix C. By design of RW, we precisely center ν_s in the target range and c/ν_i falls around 1950 nm, and in the most general design case varying R provides an independent control for continuous tuning. We test this by studying three settings of R, which deterministically shift the phase matching for spectral translation.

Adjusting the pump-laser frequency opens up the widest range of wavelength access by design of microresonator GVD. Figures 2(c) and 2(d) present OPO with tantala microresonators and a laser with $\nu_p \approx 280$ THz, demonstrating a span of signal ν_s and idler ν_i more than 200 THz, highlighting broad spectral reconfigurability and the potential to synthesize optical frequencies across various spectral bands. Here, we design tantala microresonators of 500 GHz free-spectral range and RW for slightly normal GVD in the ν_p band, eliminating OPO in that frequency range [29]. Figure 2(c) shows a typical OPO spectrum, and we observe sidebands commensurate with $\nu_s \approx 352$ THz. In Fig. 2(d), we present GVD heat maps $1/(|\Delta\nu| + 1)$ for OPO in this design regime particularly suited for wideband wavelength access. We step ν_p through the microresonator modes in the 1064 nm band, realizing variation in the spacing of ν_s and ν_i.

Bringing together the microcomb, which provides one and the same mode μ_T, and three discrete tantala devices of varying RW for spectral translation, we explore deterministic spectral-translation synthesis across the 1300 nm band [Figs. 2(e) and 2(f)] and highlight the concept of Fig. 1(a). Note that other combinations of ν_{μ_T} and ν_p can be leveraged to synthesize arbitrary frequencies via spectral translation.

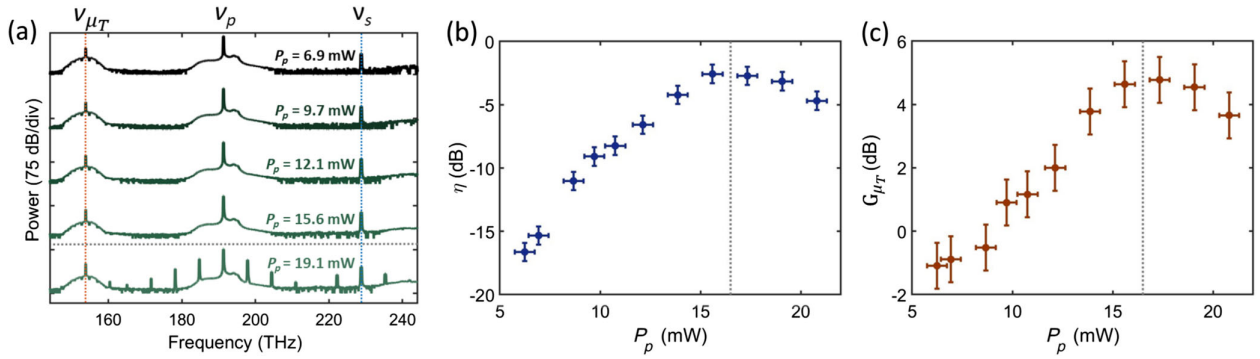

FIG. 3. Spectral-translation conversion efficiency and gain. (a) Optical spectra of spectral translation from ν_{μ_T} to ν_s (red and blue vertical dashed lines) for various on-chip pump powers P_p. The horizontal gray dashed line denotes the threshold for OPO into undesired cavity modes. (c) η as a function of P_p in dB. (c) Measured gain (G_{μ_T}) on ν_{μ_T}. The vertical gray dashed line in (b) and (c) corresponds to the horizontal line in (a).

Here, the three settings of RW enable 2 THz frequency steps of ν_s, and we utilize slight tuning of ν_p and microresonator-mode thermal tuning to optimize conversion efficiency, which in future integrated platforms could be implemented with buried heaters [38]. In particular, thermal tuning of the microresonators affects a frequency shift of -2.3 and -0.75 GHz/°C with the SiN and tantala modes at $\approx$153.9 THz, respectively. Therefore, we readily achieve optical-frequency matching of the microcomb mode and the spectral-translation idler mode, but none of these factors that control conversion efficiency impact the frequency stability of ν_s. Indeed, in Fig. 2(f), we demonstrate zero ν_s frequency error determined from 10 min duration, 0.1 s gate-time measurements.

The output power of our optical synthesizer is an important metric for applications with synthesized lasers. Overall, the output power depends on the available power of the microcomb mode μ_T and the conversion efficiency of spectral translation η, which in a nonlinear network can be quite high even with a continuous-wave pump due to high nonlinearity. Since energy is conserved in spectral translation, we naturally also expect to observe power gain (G_{μ_T}) of the mode μ_T. An additional parameter of spectral translation is the pump-laser power P_p. We characterize these aspects of our experiments by calibrating and monitoring the on-chip spectrum, especially at the frequencies ν_s, ν_P, and ν_{μ_T}; Fig. 3 presents an understanding of η and G_{μ_T} as a function of P_p. In our experimental system that couples the microcomb chip, the spectral-translation chip, and the pump lasers, the insertion loss per chip facet is $(\alpha_{\mu_T}, \alpha_p, \alpha_s) = (7.7, 4.7, 5.0) \pm 0.7$ dB. In Fig. 3(a), we present the optical spectrum of spectral translation as we vary P_p to characterize conversion efficiency. These data highlight the sparse spectrum of this nonlinear conversion process, involving only the designed waves. We analyze the spectrum in Fig. 3(a) to extract η and G_{μ_T}; see Figs. 3(b) and 3(c) (see Appendix C). In particular, we observe relatively high η [Fig. 3(b)] even with $P_p = 7$ mW, and we achieve a maximum conversion efficiency of (-2.6 ± 1.4) dB with 15 mW. We calculate the anticipated conversion efficiency at 15 mW pump power to be -2 dB, in agreement with the measurement [39]; see Appendix C. Increasing to $P_p =$ 19 mW initiates OPO in microresonator modes near the pump, owing to anomalous GVD, that slightly depletes η. Commensurate with increasing η, we also observe gain [Fig. 3(b)] that peaks at $G_{\mu_T} = 5 \pm 1$ dB. Overall, accounting for η, the chip coupling losses, and the available off-chip power in microcomb mode of 4 μW, we extract 1 μW.

IV. SYNTHESIZER VALIDATION

We expect our nonlinear network optical synthesizer to be phase-coherently linked to the reference clock, which in these experiments is a hydrogen maser. Figure 4 explores optical-frequency metrology of the synthesizer, demonstrating its accuracy, precision, and frequency-tuning capability. To assess accuracy and precision, we continuously measure $\Delta\nu_s$ in 0.1 s intervals $\tau(s)$ for a duration greater than 2 h by use of a frequency counter, which is referenced to the reference clock; see Fig. 4(a). We program the synthesizer to $\nu_s = 228.783\,502\,560\,000$ THz, which requires full optical phase stabilization of our phase locks of ν_0, ν_p, and f_{rep} (see Appendix D). The Allan deviation [Fig. 4(b)] of the $\Delta\nu_s$ data demonstrates phase-coherent operation of our synthesizer through its $4.7 \times 10^{-13}/\tau$ fractional-frequency fluctuation dependence over the range $0.1 < \tau < 10$ s. Here, we normalize frequency fluctuations to the $\approx$75 THz span of spectral translation, and the measurement uncertainty represents subhertz accuracy of the synthesizer output for continuous operation greater than 2 h. Figure 4(b) includes the measured in-loop Allan deviation of the ν_p (red) and ν_0 (dark red) phase-lock loops, as well as the Allan deviation of the f_{rep} phase-lock loop scaled by the factor μ_T. We also include a noise estimate (blue) plotted to $\tau = 100$ s with slope $1/\tau$, originating from the system's various electronic-frequency synthesizer

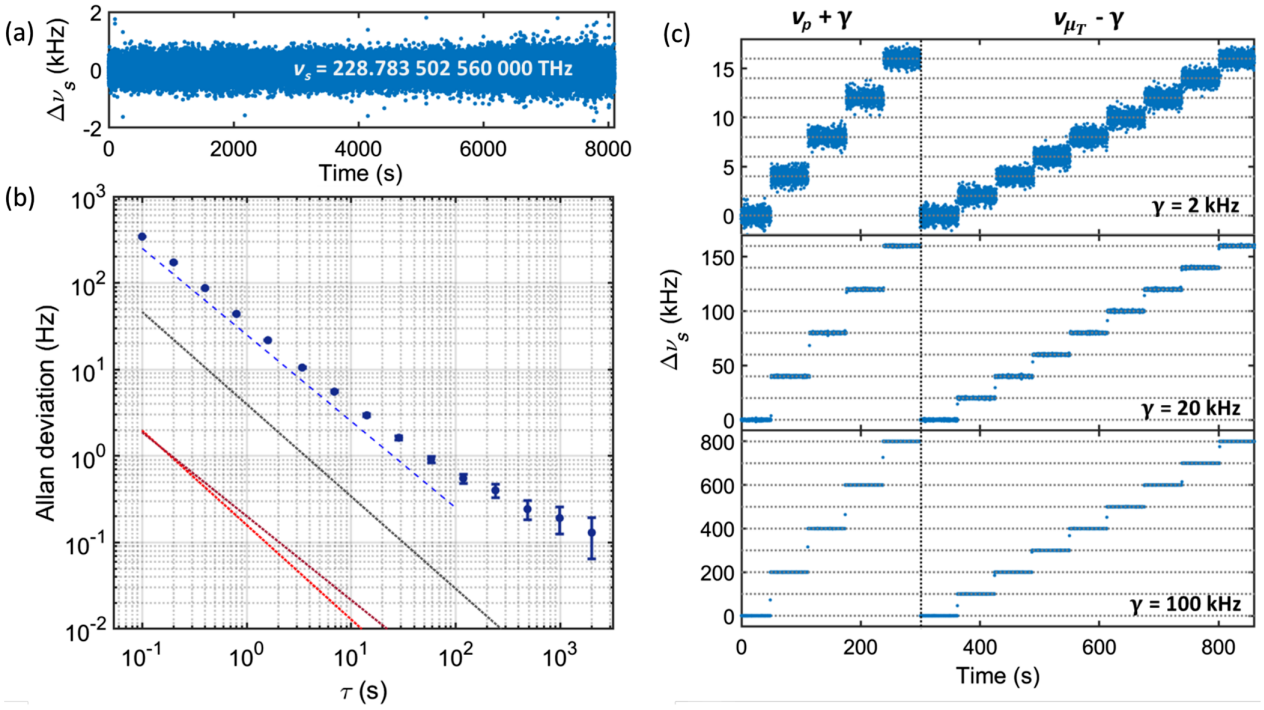

FIG. 4. Arbitrary optical-frequency synthesis. (a) Measured $\Delta\nu_s$ (gate time 100 ms) for over 2 h with a mean $\Delta\nu_s$ of −83 mHz. (b) Allan deviation of the data in (a). At $\tau = 1$ s, the Allan deviation is 35 Hz, indicating fractional stability of the spectral translation across 75 THz of 5×10^{-13}. We include the Allan deviation of the measured in-loop ν_p (red), ν_0 (dark red), and $\mu_T f_{\mathrm{rep}}$ phase locks and a noise estimate due to various electronic-synthesizer chain stabilities (blue). (c) Measured $\Delta\nu_s$ (gate time 100 ms) as we step ν_s by changing the lock point of ν_p and ν_{μ_T} by $|\gamma|$ frequency steps. The gray dashed horizontal lines denote steps of $|\gamma|$ from ν_s.

chains; see Appendix D. This estimate agrees with the measurement. The data record of $\Delta\nu_s$ indicates no frequency error at the level of 83 mHz, i.e., 1 part in 10^{16} of the synthesizer carrier frequency ν_s, which is less than the 0.1 Hz precision of this experiment. The Allan deviation of Fig. 4(b) demonstrates phase stability for over 2 h of continuous operation with a deviation from $1/\tau$ behavior for $\tau > 10$ s, which we attribute to fluctuations in the many phase locks (see Appendix D).

Our synthesizer supports ultraprecise frequency stepping [Fig. 4(c)] without any change in phase stability, GVD, or the temperature of the spectral-translation device by adjustment of the offset frequency locks of ν_p and ν_{μ_T}. Here, we indicate the frequency programming parameter as γ, which we apply to either ν_p and ν_{μ_T}. With a 3 dB variation in output power, the tuning range is approximately 400 MHz, which is consistent with total linewidth of our resonators. Importantly, γ affects an incommensurate magnitude and sign change in ν_s when applied to either ν_p and ν_{μ_T}, according to energy conservation in FWM, $\nu_s = 2\nu_p - \nu_{\mu_T}$. Figure 4(c) presents three frequency-counter records of $\Delta\nu_s$ in which we program a stepped ramp of ν_s over a period of several hundred seconds; the three separated panels present different $|\gamma|$ settings, 2, 20, and 100 kHz, applied at semiprecise 60 s intervals. A value of $\Delta\nu_s = 0$ indicates $\nu_s = 228.805\,087\,882\,250$ THz, and $\Delta\nu_s$ shows the response 2γ and γ that we anticipate as we step ν_p and ν_{μ_T}, respectively.

V. DISCUSSION AND CONCLUSION

In summary, we demonstrate an accurate and precise optical-frequency synthesizer, using a nonlinear network to overcome existing bandwidth limitations. This new architecture for optical synthesis establishes nonlinear networks of integrated microresonators in which frequency-comb generation, spectral translation, and other processes can be combined for novel system functionality. We leverage the high efficiency and widely controllable FWM phase matching in microresonators; specifically, we demonstrate ≈50% spectral-translation conversion efficiency of the microcomb and any wavelength access to a range of 200 THz. By phase stabilization of the microcomb and the spectral-translation pump laser, the synthesized output laser features an Allan deviation of 0.1 Hz, and we explore synthesizer frequency tuning in steps from 0.1 Hz to 2 THz. These factors demonstrate a complete set of functionalities for a nonlinear network optical synthesizer with

integrated microresonators and compatibility with further photonic integration. More generally, the concept of an any-wavelength laser enabled by precision control of OPO and FWM illuminates a new paradigm for access to arbitrary portions of the optical spectrum.

ACKNOWLEDGMENTS

We thank Travis Briles and Andrew Ferdinand for carefully reviewing the manuscript. This research has been funded by NIST, the DARPA DODOS and LUMOS programs, as well as AFOSR FA9550-20-1-0004 Project No. 19RT1019. This article is a contribution of the U.S. Government, not subject to U.S. copyright.

APPENDIX A: DEVICES AND NANOFABRICATIONS

Here we describe the microresonator devices used in our experiments and their fabrication. For the microcomb, we utilize SiN microresonators fabricated by Ligentec according to our designs. A 770-nm-thick SiN device layer is deposited on an oxidized silicon wafer by LPCVD, and our design layout for microresonators, waveguide couplers, and other devices is transferred to the SiN layer through deep ultraviolet (DUV) stepper lithography and reactive-ion etching. The entire wafer is clad with SiO_2 and annealed for several hours at $> 1000\,°C$ to reduce optical absorption of the SiN and SiO_2 materials. A secondary dry etching step separates the wafer to chips. With ≈8 usable DUV stepper fields, ≈30 chips per field, and up to 500 microresonators per chip, we yield a substantial number of devices for experiments on a 4-month-duration fabrication cycle. The overall process supports 200 nm feature size, especially for isolated structures like inverse tapers at chip edge. We couple light to the SiN microresonator, using a pulley coupler with pulley length 17 μm, bus waveguide width 500 nm, and gap 800 nm that enables efficient broadband coupling.

The microcomb used in our experiments has ring radius of 22.67 μm and resonator waveguide width of 1653 nm. We measure the loaded quality factor at the pump mode near 192 THz to be $\approx 1 \times 10^6$ and we pump the microcomb with ≈55 mW on chip. For a SiN layer thickness 3% thinner than our target, we find $D_2/2\pi = 2.5$ MHz, $D_3/2\pi = 94.3$ kHz, and $D_4/2\pi = -10.8$ kHz, yielding $\mu_{\mathrm{DW}} = -38,\ 73$ where the long wavelength dispersive wave is in excellent agreement with experiment. Device dimensions within 5% in thickness and RW are reasonable tolerance for deposition and electron-beam lithography. Sidewall angles can also result in deviations of the GVD from our design geometry. The SiN fabrication process results in high density of microresonators due to the DUV stepper lithography and film-thickness variation ≈5% due to the LPCVD deposition.

For the spectral translation microresonators, we utilize tantala microresonators fabricated at NIST [9,35]. A 570-nm-thick tantala film is deposited on an oxidized silicon wafer by ion-beam sputtering at FiveNine Optics, and our designs are transferred to the tantala layer through electron-beam lithography and fluorine inductively coupled plasma—reactive ion etching. For these devices the upper cladding is air; hence, following the etch we separate the wafer into chips with secondary UV laser lithography and dry etching steps. Thermal annealing in air for several hours at 500 °C reduces oxygen vacancies present in the tantala material. Our customized fabrication process yields more than 20 chips with ≈100 microresonators per chip in a focused 2-day fabrication period. Given the air cladding, for edge coupling we utilize wide inverse tapers of 2.75 μm. We couple light to the tantala microresonator using straight bus waveguides with width 750 nm and gap 500 nm. We measure loaded quality factors at 193 and 224 THz to be $\approx 3 \times 10^5$ and 1×10^6, respectively. For a tantala microresonator with residual pedestal thickness of 40 nm, we find $D_2/2\pi = 1.6$ MHz, $D_3/2\pi = 7.6$ kHz, and $D_4/2\pi = -12.2$ kHz, yielding $\mu_{\mathrm{ST}} = 43$, in good agreement with experiment. For tantala devices, we find postprocessing scanning electron microscope imaging of tantala devices reveal a remaining tantala pedestal with thicknesses of approximately tens of nanometers due to incomplete etching through the device layer. The tantala fabrication process results in moderate density of microresonators due to the electron-beam lithography and minimal film-thickness variation due to ion-beam sputtering. Because of the film hardness, residual postetch tantala pedestals result with thickness up to ≈50 nm.

APPENDIX B: BENCH-TOP LASER SYSTEMS

A commercially available tunable cw external-cavity diode laser with central wavelength 1550 nm pumps the microresonator for microcomb generation. A single-sideband modulator controls the frequency detuning of the microcomb pump laser, enabling rapid frequency tuning for soliton capture (≈6 GHz/100 nm) [40]. After single-sideband modulation and amplification via commercially available erbium-fiber amplifier, the microcomb pump laser goes through a fiber acousto-optic modulator (8 MHz bandwidth) for controlling the optical power before the chip. A second commercially available tunable cw external-cavity diode laser with central wavelength 1550 nm pumps the microresonator for spectral translation and OPO. A commercially available erbium-fiber amplifier amplifies the pump laser, and a wavelength division multiplexer combines the light with a second laser for spectral translation. For characterization of additional spectral translation devices (see Fig. 2), we employ two additional widely

tunable cw external-cavity diode lasers with central wavelengths at 1050 and 1320 nm. We amplify the 1050 nm laser with an ytterbium-doped fiber amplifier. In our experiments, we couple between standard bench-top laser and fiber components and the chips with lensed fiber and inverse-taper waveguides. Since the insertion loss from the microcomb chip to the spectral translation chip is particularly crucial to our experiments, we utilize a thulium fiber amplifier to overcome this loss.

We utilize an auxiliary 250 MHz erbium-fiber frequency comb in phase locking the synthesizer and measuring the synthesizer output as described below. The fiber frequency comb is a commercially available mode-locked laser with central wavelength 1560 nm. We amplify and spectrally broaden the frequency comb to octave spanning for self-referenced detection of f_{CEO} which is phase locked to 30 MHz and we phase lock the fourth harmonic of the directly detectable 250 MHz $f_{\mathrm{rep,aux}}$ to a reference frequency synthesizer.

APPENDIX C: DESIGN AND MEASUREMENT OF SPECTRAL TRANSLATION

GVD engineering of the microresonators uses finite-element method modeling to predict the wavelength-dependent cavity resonances. We fabricate devices with a range of geometric parameter sweeps of R (measured to the center of RW) and RW to cover the full fabrication tolerance range and ensure fabrication of the target GVD microresonator and avoid unwanted higher-order mode crossings. As described in the text, variations in waveguide thickness, residual pedestal, RW, and sidewall affect the experimental GVD. We find ≈14% of fabricated microresonators operate within our spectral target for the results presented in Fig. 2(b). We calculate $1/(|\Delta\nu|+1)$ with various geometries using the cold cavity resonances, ignoring optical-power-dependent cross- and self-phase modulation of the cavity modes. Achieving high parametric gain relies on optimizing phase matching and depends on pump power and wavelength-dependent resonator field enhancement, losses, coupling, and nonlinear coefficient. A quantitative comparison of measured conversion efficiency [Fig. 3(b)] yields −2 dB at 15 mW, where we use the measured resonator losses, mode area 0.6 $\mu\mathrm{m}^2$, and wavelength-dependent field enhancements of 19.0, 27.8, and 18.4 at signal, pump, and idler frequencies, respectively.

Wavelength division multiplexers combine the lasers for launching light onto the chip via lensed optical fibers which produces a spot size of 2 μm at 1550 nm. We precisely align the lensed optical fibers to the chip facets using translation stages and an optical microscope. Experimental measurements of η and G_{μ_T} were free running, and we record output optical spectra for various P_p with ν_p both off and on resonance. In these experiments, only ν_p is frequency tuned, and at increasing P_p, we slightly cool the tantala ring via a thermoelectric cooler to keep ν_{μ_T} on resonance when ν_p is on resonance. Cooling enables counteracting the thermo-optic coefficient-dependent shift of the resonator modes when ν_p is on resonance. We measure G_{μ_T} as the ratio of measured power at ν_{μ_T} on the optical spectrum analyzer when ν_p is on and off resonance, respectively. We measure η as the ratio of optical power at ν_s when ν_p is on resonance to optical power at ν_{μ_T} when ν_p is off resonance. Since we measure higher insertion losses at ν_{μ_T} compared to ν_s, we adjust the ratio according to the ratio of relative losses at the two wavelengths.

APPENDIX D: SYNTHESIZER PHASE LOCKING

We stabilize the synthesizer by phase locking ν_0, ν_p, and f_{rep} to the microwave clock as shown in Fig. 5. Note that fully self-referenced microcombs have been demonstrated in our previous experiments and could be used to implement the synthesizer without the auxiliary comb [19–22,40]. Indeed, the microcomb we use is derived directly from previous designs that supported phase-coherent self-referencing.

We optically heterodyne ν_0 and ν_p with the auxiliary comb to unambiguously determine their frequency. We use an optical wave meter to determine the nearest nth comb tooth of the auxiliary comb to ν_0 and ν_p. The pump lasers are phase locked to the self-referenced auxiliary comb, transferring the microwave clock stability to the microcomb pump frequencies. The Allan deviations of the measured in-loop phase locks of ν_p and ν_0 are presented in Fig. 4(b). We measure f_{rep} by passing a portion of microcomb power through an electro-optic comb which produces optical sidebands at a microwave clock referenced synthesizer

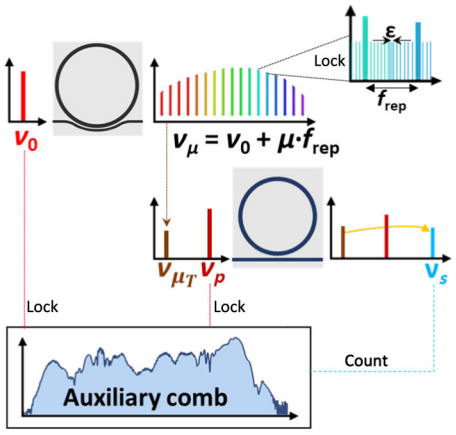

FIG. 5. Synthesizer phase locking. The pump lasers, ν_0 and ν_p, are optically heterodyned with the auxiliary comb and phase locked, enabling frequency determination and phase-stability transfer of the microwave clock. An electro-optic comb provides transfer of f_{rep} to electronically detectable ϵ for phase locking f_{rep} to the microwave clock. The synthesizer frequency ν_s is verified by counting (optical heterodyne) with the auxiliary comb.

frequency, $\nu_{\mathrm{EO}} \approx 10.018$ GHz [41,42]. The electro-optic comb generates 100 optical sidebands which fill in the ≈1 THz f_{rep}. We optically filter a 0.1 nm bandwidth centered between two microcomb modes (≈1541 nm) and measure the optical heterodyne beat note (ϵ) of the 50th optical sideband from either neighboring microcomb frequency. Then f_{rep} is determined by $100\nu_{\mathrm{EO}} + \epsilon$ and we phase lock f_{rep} by controlling the microcomb pump power with an acousto-optic modulator described above. The frequency noise on ν_{μ_T} scales with μ_T times the frequency noise of f_{rep}, which is plotted in Fig. 4(b). We phase lock a tunable external-cavity diode laser with central wavelength 1320 nm and milliwatts of optical power to the auxiliary comb to use as a helper laser with frequency ν_h to boost the signal-to-noise ratio of the final rf beat note to ≈35 dB for frequency counting of ν_s. We measure the in-loop phase locks of ν_h, ν_0, ν_p, and f_{rep} and find all to have frequency error below 600 μHz. The phase lock of f_{rep} has $|\Delta\nu_s| = 93.3$ μHz measured over 15 min. Multiplying this frequency error across 75 THz of spectral translation yields frequency error < 10 mHz, consistent with our measurements.

These measurements incorporate the entire optical bandwidth of our spectral-translation synthesizer and self-referenced auxiliary comb, including their electronics for phase stabilization; hence, the overall stability of the synthesizer relies on several phase locks and the optical path length stability of the system. We estimate the added frequency noise of the ν_s Allan deviation [Fig. 4(b)] arising from the electronic-frequency synthesizer chains in the experiment, including dominate contributions from the auxiliary and microcomb repetition frequencies. We note that temperature fluctuations in the room push the locks of ν_p and ν_0 to unstable ranges of the locking electronics. Also, phase locking on hours-long timescales leads to drifting of the optical path length and the lensed optical fibers at the chip facets, resulting in signal-to-noise variations due to changing optical power, affecting the stability of the phase locks.

[1] N. Picqué and T. W. Hänsch, *Mid-ir spectroscopic sensing*, Opt. Photonics News **30**, 26 (2019).

[2] B. P. Abbott *et al.* (LIGO Scientific Collaboration and Virgo Collaboration), *GW170817: Observation of Gravitational Waves from a Binary Neutron Star Inspiral*, Phys. Rev. Lett. **119**, 161101 (2017).

[3] J. Grotti, S. Koller, S. Vogt, S. Häfner, U. Sterr, C. Lisdat, H. Denker, C. Voigt, L. Timmen, A. Rolland *et al.*, *Geodesy and Metrology with a Transportable Optical Clock*, Nat. Phys. **14**, 437 (2018).

[4] P. J. Schroeder, R. J. Wright, S. Coburn, B. Sodergren, K. C. Cossel, S. Droste, G. W. Truong, E. Baumann, F. R. Giorgetta, I. Coddington *et al.*, *Dual Frequency Comb Laser Absorption Spectroscopy in a 16 MW Gas Turbine Exhaust*, Proc. Combust. Inst. **36**, 4565 (2017).

[5] W. F. McGrew, X. Zhang, H. Leopardi, R. Fasano, D. Nicolodi, K. Beloy, J. Yao, J. A. Sherman, S. A. Schaeffer, J. Savory *et al.*, *Towards the Optical Second: Verifying Optical Clocks at the SI Limit*, Optica **6**, 448 (2019).

[6] T. W. Hänsch, *Nobel Lecture: Passion for Precision*, Rev. Mod. Phys. **78**, 1297 (2006).

[7] J. L. Hall, *Nobel Lecture: Defining and Measuring Optical Frequencies*, Rev. Mod. Phys. **78**, 1279 (2006).

[8] J. A. Black, R. Streater, K. F. Lamee, D. R. Carlson, S.-P. Yu, and S. B. Papp, *Group-Velocity-Dispersion Engineering of Tantala Integrated Photonics*, Opt. Lett. **46**, 817 (2021).

[9] S.-P. Yu, D. C. Cole, H. Jung, G. T. Moille, K. Srinivasan, and S. B. Papp, *Spontaneous Pulse Formation in Edgeless Photonic Crystal Resonators*, Nat. Photonics **15**, 461 (2021).

[10] A. D. Ludlow, M. M. Boyd, J. Ye, E. Peik, and P. O. Schmidt, *Optical Atomic Clocks*, Rev. Mod. Phys. **87**, 637 (2015).

[11] F. R. Giorgetta, W. C. Swann, L. C. Sinclair, E. Baumann, I. Coddington, and N. R. Newbury, *Optical Two-Way Time and Frequency Transfer over Free Space*, Nat. Photonics **7**, 434 (2013).

[12] A. Schliesser, N. Picqué, and T. W. Hänsch, *Mid-Infrared Frequency Combs*, Nat. Photonics **6**, 440 (2012).

[13] J. D. Jost, J. L. Hall, and J. Ye, *Continuously Tunable, Precise, Single Frequency Optical Signal Generator*, Opt. Express **10**, 515 (2002).

[14] S. A. Diddams, K. Vahala, and T. Udem, *Optical Frequency Combs: Coherently Uniting the Electromagnetic Spectrum*, Science **369**, eaay3676 (2020).

[15] T. J. Kippenberg, A. L. Gaeta, M. Lipson, and M. L. Gorodetsky, *Dissipative Kerr Solitons in Optical Microresonators*, Science **361**, eaan8083 (2018).

[16] Q. Li, T. C. Briles, D. A. Westly, T. E. Drake, J. R. Stone, B. R. Ilic, S. A. Diddams, S. B. Papp, and K. Srinivasan, *Stably Accessing Octave-Spanning Microresonator Frequency Combs in the Soliton Regime*, Optica **4**, 193 (2017).

[17] T. C. Briles, S.-P. Yu, T. E. Drake, J. R. Stone, and S. B. Papp, *Generating Octave-Bandwidth Soliton Frequency Combs with Compact Low-Power Semiconductor Lasers*, Phys. Rev. Appl. **14**, 014006 (2020).

[18] T. E. Drake, J. R. Stone, T. C. Briles, and S. B. Papp, *Thermal Decoherence and Laser Cooling of Kerr Microresonator Solitons*, Nat. Photonics **14**, 480 (2020).

[19] T. C. Briles, J. R. Stone, T. E. Drake, D. T. Spencer, C. Fredrick, Q. Li, D. Westly, B. Ilic, K. Srinivasan, S. A. Diddams *et al.*, *Interlocking Kerr-Microresonator Frequency Combs for Microwave to Optical Synthesis*, Opt. Lett. **43**, 2933 (2018).

[20] D. T. Spencer, T. Drake, T. C. Briles, J. Stone, L. C. Sinclair, C. Fredrick, Q. Li, D. Westly, B. R. Ilic, A. Bluestone *et al.*, *An Optical-Frequency Synthesizer Using Integrated Photonics*, Nature (London) **557**, 81 (2018).

[21] T. E. Drake, T. C. Briles, J. R. Stone, D. T. Spencer, D. R. Carlson, D. D. Hickstein, Q. Li, D. Westly, K. Srinivasan, S. A. Diddams, and S. B. Papp, *Terahertz-Rate Kerr-Microresonator Optical Clockwork*, Phys. Rev. X **9**, 031023 (2019).

[22] Z. L. Newman, V. Maurice, T. Drake, J. R. Stone, T. C. Briles, D. T. Spencer, C. Fredrick, Q. Li, D. Westly, B. R. Ilic *et al.*, *Architecture for the Photonic Integration of an Optical Atomic Clock*, Optica **6**, 680 (2019).

[23] Q. Lin, T. Johnson, R. Perahia, C. Michael, and O. Painter, *A Proposal for Highly Tunable Optical Parametric Oscillation in Silicon Micro-Resonators*, Opt. Express **16**, 10596 (2008).

[24] K. M. Kiani, H. M. Mbonde, H. C. Frankis, R. Mateman, A. Leinse, A. P. Knights, and J. D. Bradley, *Four-Wave Mixing in High-Q Tellurium-Oxide-Coated Silicon Nitride Microring Resonators*, OSA Contin. **3**, 3497 (2020).

[25] Y. Tang, Z. Gong, X. Liu, and H. X. Tang, *Widely Separated Optical Kerr Parametric Oscillation in AlN Microrings*, Opt. Lett. **45**, 1124 (2020).

[26] M. A. Guidry, K. Y. Yang, D. M. Lukin, A. Markosyan, J. Yang, M. M. Fejer, and J. Vučković, *Optical Parametric Oscillation in Silicon Carbide Nanophotonics*, Optica **7**, 1139 (2020).

[27] C. Wang, Z. Fang, A. Yi, B. Yang, Z. Wang, L. Zhou, C. Shen, Y. Zhu, Y. Zhou, R. Bao *et al.*, *High-Q Microresonators on 4H-Silicon-Carbide-on-Insulator Platform for Nonlinear Photonics*, Light Sci. Appl. **10**, 1 (2021).

[28] X. Lu, G. Moille, Q. Li, D. A. Westly, A. Singh, A. Rao, S.-P. Yu, T. C. Briles, S. B. Papp, and K. Srinivasan, *Efficient Telecom-to-Visible Spectral Translation through Ultralow Power Nonlinear Nanophotonics*, Nat. Photonics **13**, 593 (2019).

[29] X. Lu, G. Moille, A. Rao, D. A. Westly, and K. Srinivasan, *On-Chip Optical Parametric Oscillation into the Visible: Generating Red, Orange, Yellow, and Green from a Near-Infrared Pump*, Optica **7**, 1417 (2020).

[30] T. J. Kippenberg, S. M. Spillane, and K. J. Vahala, *Kerr-Nonlinearity Optical Parametric Oscillation in an Ultrahigh-Q Toroid Microcavity*, Phys. Rev. Lett. **93**, 083904 (2004).

[31] Z. Ye, P. Zhao, K. Twayana, M. Karlsson, V. Torres-Company, and P. A. Andrekson, *Overcoming the Quantum Limit of Optical Amplification in Monolithic Waveguides*, Sci. Adv. **7**, eabi8150 (2021).

[32] R. R. Domeneguetti, Y. Zhao, X. Ji, M. Martinelli, M. Lipson, A. L. Gaeta, and P. Nussenzveig, *Parametric Sideband Generation in CMOS-Compatible Oscillators from Visible to Telecom Wavelengths*, Optica **8**, 316 (2021).

[33] N. L. B. Sayson, T. Bi, V. Ng, H. Pham, L. S. Trainor, H. G. Schwefel, S. Coen, M. Erkintalo, and S. G. Murdoch, *Octave-Spanning Tunable Parametric Oscillation in Crystalline Kerr Microresonators*, Nat. Photonics **13**, 701 (2019).

[34] S. Fujii, S. Tanaka, M. Fuchida, H. Amano, Y. Hayama, R. Suzuki, Y. Kakinuma, and T. Tanabe, *Octave-Wide Phase-Matched Four-Wave Mixing in Dispersion-Engineered Crystalline Microresonators*, Opt. Lett. **44**, 3146 (2019).

[35] H. Jung, S.-P. Yu, D. R. Carlson, T. E. Drake, T. C. Briles, and S. B. Papp, *Tantala Kerr Nonlinear Integrated Photonics*, Optica **8**, 811 (2021).

[36] K. F. Lamee, D. R. Carlson, Z. L. Newman, S.-P. Yu, and S. B. Papp, *Nanophotonic Tantala Waveguides for Supercontinuum Generation Pumped at 1560 nm*, Opt. Lett. **45**, 4192 (2020).

[37] V. Brasch, M. Geiselmann, T. Herr, G. Lihachev, M. H. P. Pfeiffer, M. L. Gorodetsky, and T. J. Kippenberg, *Photonic Chip–Based Optical Frequency Comb Using Soliton Cherenkov Radiation*, Science **351**, 357 (2016).

[38] G. Moille, D. Westly, E. F. Perez, M. Metzler, G. Simelgor, and K. Srinivasan, *Integrated Buried Heaters for Efficient Spectral Control of Air-Clad Microresonator Frequency Combs*, APL Photonics **7**, 126104 (2022).

[39] P. Absil, J. Hryniewicz, B. Little, P. Cho, R. Wilson, L. Joneckis, and P.-T. Ho, *Wavelength Conversion in GaAs Micro-Ring Resonators*, Opt. Lett. **25**, 554 (2000).

[40] J. R. Stone, T. C. Briles, T. E. Drake, D. T. Spencer, D. R. Carlson, S. A. Diddams, and S. B. Papp, *Thermal and Nonlinear Dissipative-Soliton Dynamics in Kerr-Microresonator Frequency Combs*, Phys. Rev. Lett. **121**, 063902 (2018).

[41] P. Del'Haye, S. B. Papp, and S. A. Diddams, *Hybrid Electro-Optically Modulated Microcombs*, Phys. Rev. Lett. **109**, 263901 (2012).

[42] D. R. Carlson, D. D. Hickstein, W. Zhang, A. J. Metcalf, F. Quinlan, S. A. Diddams, and S. B. Papp, *Ultrafast Electro-Optic Light with Subcycle Control*, Science **361**, 1358 (2018).